

Enhancing 3D Semantic Scene Completion with Refinement Module

Dunxing Zhang^{3,†}, **Jiachen Lu**^{3,†}, **Han Yang**^{1,2,*}, **Lei Bao**^{1,2} and **Bo Song**^{1,2}

¹*National Science Center for Earthquake Engineering, Tianjin University, Tianjin 300350, China*

²*School of Civil Engineering, Tianjin University, Tianjin 300350, China*

³*Chair of Robotics, Artificial Intelligence and Real-time Systems, Technical University of Munich, Munich, Germany*

Correspondence*:

Han Yang

professorhansolo@tju.edu.cn

ABSTRACT

We propose ESSC-RM, a plug-and-play **Enhancing** framework for **Semantic Scene Completion** with a **Refinement Module**, which can be seamlessly integrated into existing SSC models. ESSC-RM operates in two phases: a baseline SSC network first produces a coarse voxel prediction, which is subsequently refined by a 3D U-Net-based **Prediction Noise-Aware Module** (PNAM) and Voxel-level Local Geometry Module (VLGM) under multiscale supervision. Experiments on SemanticKITTI show that ESSC-RM consistently improves semantic prediction performance. When integrated into CGFormer and MonoScene, the mean IoU increases from 16.87% to 17.27% and from 11.08% to 11.51%, respectively. These results demonstrate that ESSC-RM serves as a general refinement framework applicable to a wide range of SSC models. Project page: <https://github.com/LuckyMax0722/ESSC-RM> and <https://github.com/LuckyMax0722/VLGSSC>.

1 INTRODUCTION

Accurate 3D scene understanding is fundamental to autonomous driving, robotics, and embodied perception, where downstream tasks such as detection, reconstruction, mapping, and planning rely on complete geometric and semantic representations of the environment Guo et al. (2019); Yurtsever et al. (2020); Cao et al. (2022); Ma et al. (2022); Zhao et al. (2024a); Cao et al. (2024b). However, real-world sensors (LiDAR and RGB cameras) provide only sparse, noisy, and partial observations due to occlusions, limited resolution, restricted field of view, and missing depth information, resulting in incomplete voxelized scenes Roldao et al. (2021); Cao et al. (2024c). To address this, 3D semantic scene completion (SSC) aims to jointly infer voxel occupancy and semantic labels, a task first formalized by SSCNet Song et al. (2016).

Despite extensive progress in both LiDAR-based Roldão et al. (2020); Yan et al. (2020); Xia et al. (2023); Jang et al. (2024) and vision-based SSC Cao and de Charette (2021); Li et al. (2023b); Jiang et al. (2023); Tang et al. (2023), a considerable gap remains between predictions and ground truth. LiDAR-based models suffer from sparsity; BEV-based methods Yang et al. (2021) lose fine-grained details; RGB-based approaches degrade due to depth ambiguity and unclear 2D–3D projection Lee et al. (2024); and distillation pipelines depend heavily on task-specific teacher designs Xia et al. (2023). Moreover, SSC architectures differ substantially, making it difficult to develop a unified refinement strategy that generalizes across models without modifying their internal structures.

To bridge these limitations, this thesis proposes **ESSC-RM**, a unified coarse-to-fine refinement framework that directly enhances the voxel predictions of arbitrary SSC models. ESSC-RM performs multi-scale geometric–semantic aggregation, integrates auxiliary priors, and introduces a model-agnostic refinement pipeline that requires no architectural modification to the baseline. It supports both end-to-end joint training and fully independent plug-and-play deployment.

The main contributions of this thesis are as follows:

- We introduce **ESSC-RM**, a general refinement framework designed to improve heterogeneous SSC baselines via coarse-to-fine multi-scale error reduction, applicable to both LiDAR-based and vision-based methods.
- We develop two complementary training paradigms: a *joint training* mode that co-optimizes the refinement and baseline networks, and a *separate training* mode enabling true plug-and-play enhancement without modifying the original SSC architecture.
- We propose a neighborhood-attention-based multi-scale aggregation module that adaptively fuses geometric and semantic features, improving voxel-level reasoning across scales.
- We introduce a novel vision–language guidance module that injects text-derived semantic priors to compensate for missing geometric cues and ambiguous visual projections, enhancing cross-modal scene understanding.
- Extensive experiments on SemanticKITTI Behley et al. (2019) demonstrate that **ESSC-RM** consistently improves strong baselines such as CGFormer and MonoScene, validating its generality, flexibility, and effectiveness.

2 RELATED WORK

In this section, we review *LiDAR- and camera-based 3D perception*, then summarize advances in *3D SSC*, and finally discuss recent progress in *vision–language models (VLMs)* and *text-driven multimodal fusion*.

2.1 LiDAR-based 3D Perception

LiDAR provides accurate 3D geometry for autonomous driving perception, enabling detection, tracking, and mapping, and has become a core sensing modality Guo et al. (2019); Yurtsever et al. (2020); Ma et al. (2022); Zhao et al. (2024a); Wu et al. (2022); Lin and Wu (2025).

Early point-based and voxel-based detectors—PointNet Qi et al. (2016), VoxelNet Zhou and Tuzel (2017), SECOND Yan et al. (2018), PointPillars Lang et al. (2018), PointRCNN Shi et al. (2018), PV-RCNN Shi et al. (2019), and Voxel R-CNN Deng et al. (2020)—established effective feature extraction paradigms. Tracking frameworks such as AB3DMOT Weng et al. (2020) and Cho and Kim (2023) leverage motion models and geometric association. Semantic segmentation approaches including PointNet++ Qi et al. (2017), RangeNet++ Milioto et al. (2019), and Cylinder3D Zhou et al. (2020) demonstrate point-based, projection-based, and cylindrical-voxel inference strategies.

2.2 Camera-based 3D Perception

Camera-based perception offers a cost-efficient alternative with rich semantic cues. Monocular approaches extend 2D detectors Brazil and Liu (2019); Duan et al. (2019); Manhardt et al. (2018) or rely on pseudo-depth and geometric priors Xu and Chen (2018); Wang et al. (2018); Zia et al. (2014); Mousavian et al. (2016); Hu et al. (2018), yet remain affected by depth ambiguity. Stereo-based methods Chang and Chen (2018); Li et al. (2019); You et al. (2019); Chen et al. (2020) mitigate this by enforcing geometric consistency Mao et al. (2023).

With multi-camera setups becoming standard, multi-view 3D detection methods have evolved rapidly. LSS-based pipelines Phlion and Fidler (2020); Huang et al. (2021) lift image features to Bird’s-Eye View (BEV), while transformer-based designs such as DETR3D Wang et al. (2021) and BEVFormer Li et al. (2022b) aggregate cross-view features using 3D object queries. Spatiotemporal attention mechanisms Vaswani et al. (2017); Doll et al. (2022); Mao et al. (2023) further enhance robustness.

2.3 Semantic Scene Completion

SSC jointly predicts occupancy and voxel-level semantics. SSCNet Song et al. (2016) established the task on indoor data Silberman et al. (2012); outdoor datasets such as KITTI and SemanticKITTI Geiger et al. (2012); Behley et al. (2019, 2021); Li et al. (2024) introduce sparsity and large-scale variability.

2.4 Vision–Language Models

Vision–language models (VLMs) provide strong semantic priors through aligned image–text representations Liu et al. (2025). CLIP Radford et al. (2021) and EVACLIP Sun et al. (2023, 2024) learn powerful contrastive embeddings, while LongCLIP Zhang et al. (2024) and JinaCLIP Koukounas et al. (2024a,b) improve long-text modeling.

Models such as BLIP2 Li et al. (2023a), InstructBLIP Dai et al. (2023), MiniGPT-4 Zhu et al. (2023), and LLaVA Liu et al. (2023a, 2024) leverage frozen Large Language Models (LLMs) to build efficient multimodal reasoning pipelines OpenAI et al. (2024). Text-conditioned segmentation models such as LSeg Li et al. (2022a) and Grounded-SAM Ren et al. (2024) further highlight the utility of text in perception tasks Liu et al. (2023b); Kirillov et al. (2023).

2.5 Multimodal Fusion and Text Modality

Multimodal fusion traditionally combines 3D geometry (LiDAR, stereo) with rich 2D semantics. With the emergence of LLMs and VLMs, text has become a scalable, low-cost semantic modality for describing road scenes Li and Tang (2024); Liu et al. (2025).

Attention-based fusion Vaswani et al. (2017); Cao et al. (2021)—as in Xu et al. (2020); Cao et al. (2024d); Wang et al. (2025b)—captures long-range cross-modal dependencies but can be computationally heavy. Learnable fusion strategies such as Text-IF Yi et al. (2024) and VLScene Wang et al. (2025a) use trainable coefficients to balance visual and linguistic cues.

3 METHODOLOGY

ESSC-RM refines the coarse voxel predictions produced by any SSC backbone. We now present the problem formulation and describe the architecture components of our refinement module, including the 3D U-Net backbone, the progressive neighbourhood attention module (PNAM), and the visual–language guidance module (VLGM), as illustrated in Figure 1.

3.1 Problem Statement

Given an RGB image $\mathbf{I}_t \in \mathbb{R}^{H \times W \times 3}$ and a LiDAR point cloud $\mathbf{P}_t \in \mathbb{R}^{N \times 3}$ at time t , 3D SSC aims to predict a dense semantic voxel grid $\hat{\mathbf{Y}}_t \in \{c_0, c_1, \dots, c_C\}^{H \times W \times Z}$ defined in the vehicle coordinate system, where each voxel is either empty (c_0) or belongs to one of the C semantic classes $\{c_1, \dots, c_C\}$ and H, W, Z denote the voxel grid dimensions. A standard SSC backbone learns $\hat{\mathbf{Y}}_t = f_\theta(\mathbf{I}_t, \mathbf{P}_t)$, but the coarse prediction $\hat{\mathbf{Y}}_t$ often exhibits broken surfaces, incomplete structures, and semantic confusions. We therefore introduce a refinement module g_ϕ that treats $\hat{\mathbf{Y}}_t$ as a noisy discrete volume and outputs a refined prediction $\hat{\mathbf{Y}}'_t = g_\phi(\hat{\mathbf{Y}}_t, \text{aux})$, where aux denotes additional cues (multi-scale voxel features and text semantics) extracted within the refinement module. The objective is to bring $\hat{\mathbf{Y}}'_t$ closer to the ground truth \mathbf{Y}_t in both geometry and semantics while remaining compatible with heterogeneous SSC backbones.

3.2 Overall Architecture

As shown in Figure 1, ESSC-RM has two decoupled parts:

- **SSC backbone:** maps $(\mathbf{I}_t, \mathbf{P}_t)$ to a coarse voxel grid $\hat{\mathbf{Y}}_t$.
- **Refinement module:** operates purely in voxel space, refining $\hat{\mathbf{Y}}_t$ into $\hat{\mathbf{Y}}'_t$ using multi-scale U-Net features, neighbourhood attention, and visual–language guidance.

This separation allows us to plug in backbones of different quality while focusing the design of g_ϕ on correcting geometric and semantic errors at the voxel level using additional structural and semantic cues.

3.3 SSC Backbone

ESSC-RM is model-agnostic and can refine the output of any SSC backbone. To demonstrate generality, we instantiate two monocular SSC models with different coarse prediction qualities: CGFormer Tang et al.

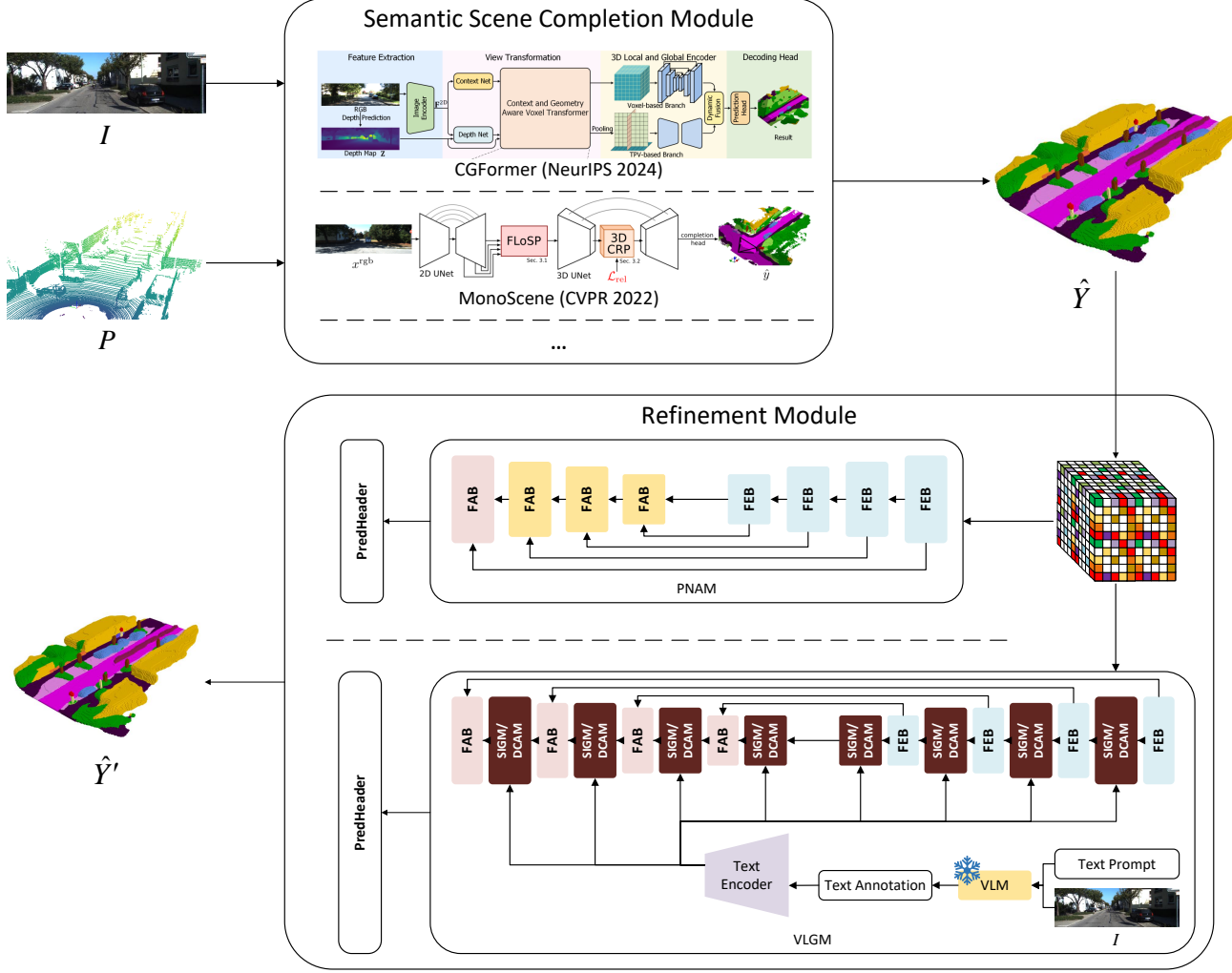


Figure 1. Overall architecture of ESSC-RM. An SSC backbone first predicts a coarse semantic voxel grid from image and/or LiDAR input. The refinement module embeds the discrete voxel labels into continuous features and processes them with a 3D U-Net enhanced by PNAM and VLGM, finally producing a refined semantic volume \hat{Y}' .

(2023) and MonoScene Cao and de Charette (2021). CGFormer represents a strong backbone with accurate voxel lifting, while MonoScene produces notably noisier volumes, providing a more challenging setting for refinement. All architectural details follow the original papers, as our refinement module does not modify or depend on the internal design of the backbone.

3.4 3D U-Net Refinement Backbone

The refinement module receives the coarse discrete volume \hat{Y} and must (i) map it into a continuous feature space, (ii) aggregate multi-scale contextual information, and (iii) reconstruct a refined voxel grid \hat{Y}' . To accomplish these steps, we adopt a three-dimensional U-shaped neural network (3D U-Net) backbone Çiçek et al. (2016); Ronneberger et al. (2015), whose overall encoder–bottleneck–decoder structure is illustrated in Figure 2. The specific computational blocks that constitute the encoder and decoder, namely the feature encoding block (FEB) and the feature aggregation block (FAB), are detailed in Figure 3.

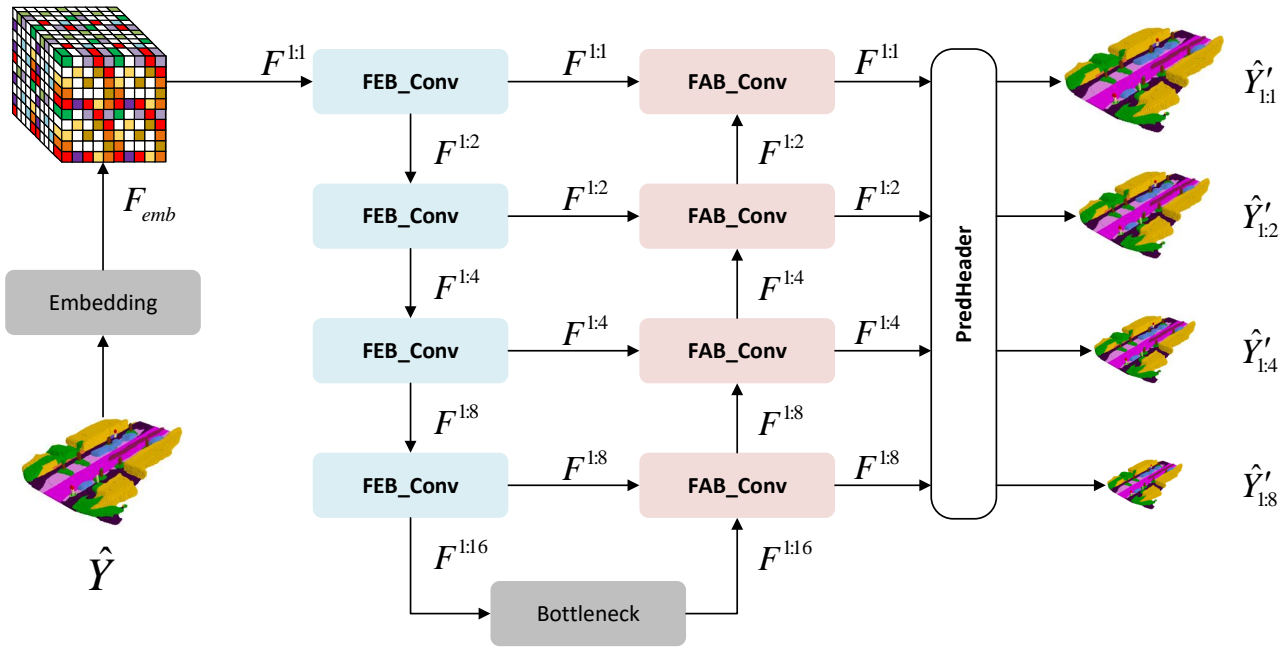


Figure 2. Three-dimensional U-shaped neural network (3D U-Net) backbone used in the refinement module. The encoder consists of stacked feature encoding blocks (FEBs) that progressively downsample the input and extract multi-scale features, a bottleneck aggregates global context, and the decoder consists of stacked feature aggregation blocks (FABs) that progressively upsample the features and predict semantic voxel outputs at four spatial scales.

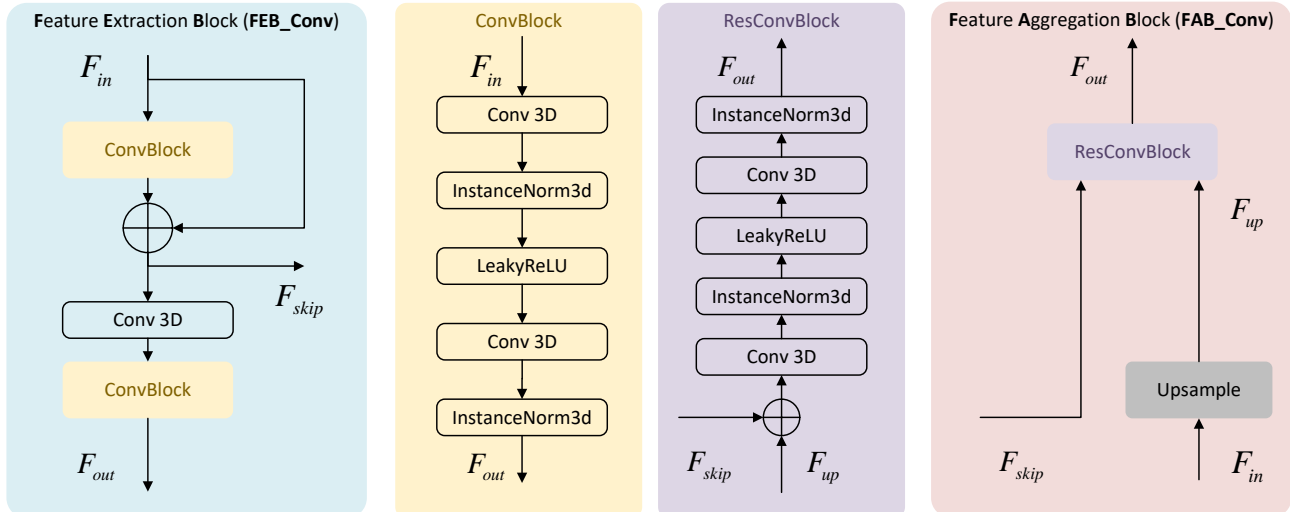


Figure 3. Core components of the three-dimensional U-shaped neural network (3D U-Net). The feature encoding block (FEB) applies three-dimensional convolutions, normalization, and residual connections to encode geometric and semantic information, while the feature aggregation block (FAB) upsamples low-resolution features and fuses them with skip connections to recover fine spatial details.

3.4.1 Voxel Embedding and Encoder–Decoder

We first embed the discrete labels of \hat{Y} into a continuous feature map:

$$F_{\text{emb}} = \text{Embedding}(\hat{Y}), \quad (1)$$

where $F_{\text{emb}} \in \mathbb{R}^{C \times H \times W \times Z}$. A $1 \times 1 \times 1$ 3D convolution then produces the input feature:

$$F_{\text{in}} = \text{Conv}_{\text{in}}(F_{\text{emb}}). \quad (2)$$

The encoder uses four stacked feature encoding blocks (FEBs) (Figure 3) to extract multi-scale features $F^{1:s}$ at progressively lower resolutions. For a voxel grid of size $H \times W \times Z$ and feature dimension G , the encoder outputs

$$F^{1:s} \in \mathbb{R}^{G \times \frac{H}{s} \times \frac{W}{s} \times \frac{Z}{s}}, \quad s \in \{1, 2, 4, 8, 16\}. \quad (3)$$

A bottleneck processes $F^{1:16}$, and the decoder then upsamples via four stacked feature aggregation blocks (FABs), followed by a shared prediction head that produces voxel logits at multiple scales:

$$\hat{Y}'_{1:s} \in \mathbb{R}^{C \times \frac{H}{s} \times \frac{W}{s} \times \frac{Z}{s}}, \quad s \in \{1, 2, 4, 8\}, \quad (4)$$

where C is the number of semantic classes. At inference time, we use

$$\hat{Y}' = \arg \max_c \hat{Y}'_{1:1,c} \quad (5)$$

as the final refined semantic voxel prediction.

3.4.2 Feature Encoding Block (FEB)

Each FEB refines features at a given scale and produces both a skip feature and a downsampled feature. As in Figure 3, an FEB applies two 3D convolutions with InstanceNorm3D Ulyanov et al. (2016) and LeakyReLU Xu et al. (2015), followed by a residual skip and a stride-2 convolution:

$$\begin{cases} F_{\text{skip}}^{1:\ell} = \text{ConvBlock}(F_{\text{in}}^{1:\ell}) + F_{\text{in}}^{1:\ell}, \\ F^{1:2\ell} = \text{Conv}_{2 \times 2 \times 2}(F_{\text{skip}}^{1:\ell}), \\ F_{\text{out}}^{1:2\ell} = \text{ConvBlock}(F^{1:2\ell}), \end{cases} \quad \forall \ell \in \{1, 2, 4, 8\}. \quad (6)$$

3.4.3 Feature Aggregation Block (FAB) and Multi-scale Supervision

Each FAB upsamples low-resolution features and fuses them with encoder skip features:

$$\begin{cases} F_{\text{up}}^{1:2\ell} = \text{UpSample}(F_{\text{in}}^{1:2\ell}), \\ F_{\text{out}}^{1:\ell} = \text{ResConvBlock}(F_{\text{skip}}^{1:\ell}, F_{\text{up}}^{1:2\ell}), \end{cases} \quad \forall \ell \in \{1, 2, 4, 8\}. \quad (7)$$

Following PaSCo Cao et al. (2024a), each decoder feature map $F_{\text{out}}^{1:\ell}$ is mapped to logits by a $1 \times 1 \times 1$ 3D convolution:

$$\hat{Y}'_{1:\ell} = \text{PredHead}(F_{\text{out}}^{1:\ell}), \quad \forall \ell \in \{1, 2, 4, 8\}, \quad (8)$$

and all scales are supervised during training. This encourages coarse-to-fine refinement and stabilises optimisation.

3.5 Progressive Neighborhood Attention Module (PNAM)

Purely convolutional decoders aggregate context only within fixed local windows, limiting their ability to capture long-range and structure-aware voxel relations. To address this, we integrate the Progressive Neighborhood Attention Module (PNAM) Liu et al. (2023c) into the decoder of our refinement network.

As illustrated in Figure 4, the FABs at scales 1:2, 1:4, and 1:8 are replaced with PNA-based FABs, while the finest-scale FAB remains convolutional for efficiency. PNAM enhances multi-scale voxel reasoning by combining global self-attention Vaswani et al. (2017) with localized neighborhood aggregation Hassani and Shi (2022); Hassani et al. (2023, 2024).

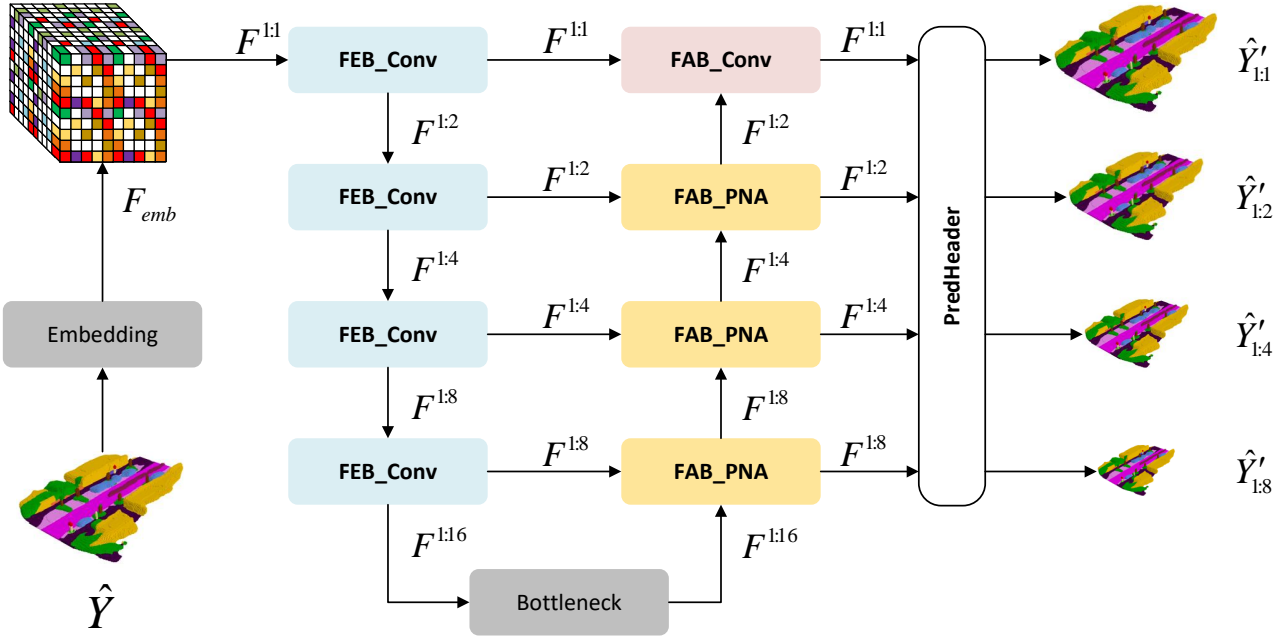


Figure 4. Progressive Neighborhood Attention U-Net (PNA U-Net) Liu et al. (2023c). PNAM replaces the feature aggregation blocks (FABs) at intermediate scales (1:2, 1:4, 1:8) with attention-based FABs, while the finest-scale FAB remains convolutional for efficiency.

3.5.1 PNA-based Feature Aggregation Block

As illustrated in Figure 5, a PNA-based FAB consists of two branches: (1) a self-attention (SA) branch operating on F_{up} , and (2) a neighborhood cross-attention (NCA) branch operating between F_{skip} and F_{up} .

Given the upsampled feature $F_{\text{up}}^{1:\ell}$ and the corresponding skip feature $F_{\text{skip}}^{1:\ell}$, the two attention responses are computed as:

$$F_{\text{self}}^{1:\ell} = \text{SA}(F_{\text{up}}^{1:\ell}), \quad F_{\text{cross}}^{1:\ell} = \text{NCA}(F_{\text{skip}}^{1:\ell}, F_{\text{up}}^{1:\ell}),$$

for $\ell \in \{2, 4, 8\}$. The outputs are fused and refined via normalization and a lightweight feed-forward network:

$$F_{\text{out}}^{1:\ell} = \text{FFN}(\text{Norm}(F_{\text{self}}^{1:\ell} + F_{\text{cross}}^{1:\ell})).$$

3.5.2 Self-Attention (SA)

SA refines the upsampled voxel features by capturing long-range dependencies. Following the standard multi-head attention formulation Vaswani et al. (2017), we use 1^3 and depthwise 3^3 convolutions to compute Q , K , V , followed by attention and a residual FFN. This propagates global geometric–semantic cues, compensating for missing structures in the coarse prediction.

3.5.3 Neighborhood Cross-Attention (NCA)

NCA enforces local geometric consistency. Inspired by the NATTEN family of neighborhood attention operators Hassani and Shi (2022); Hassani et al. (2023, 2024), it restricts attention to a 3D neighborhood window, enabling each voxel to aggregate high-confidence structural cues from spatially adjacent voxels. This makes PNAM particularly effective at restoring fine structures such as object boundaries and thin geometry.

Overall, PNAM strengthens the refinement network’s ability to jointly model global context and local voxel continuity across scales.

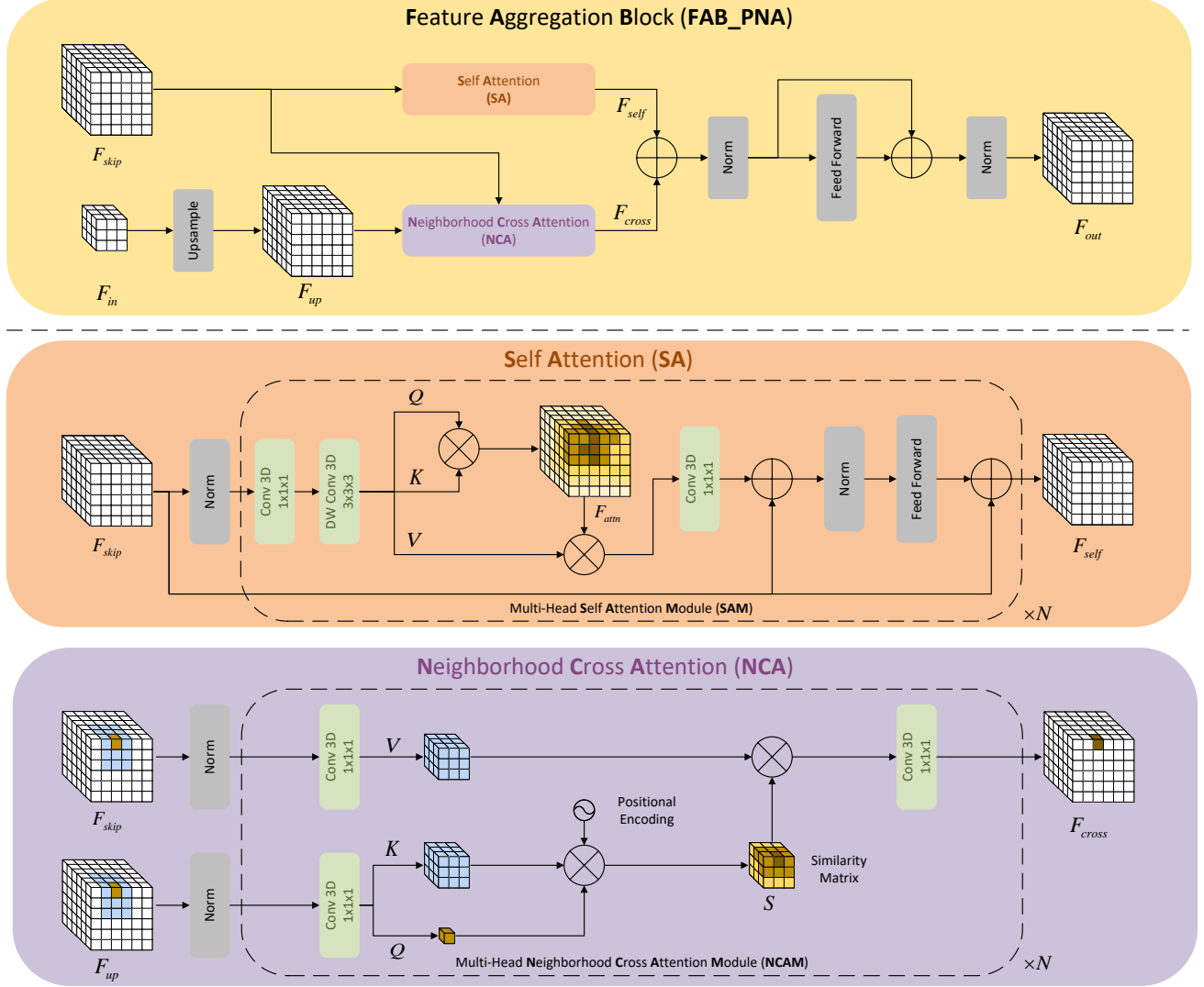


Figure 5. Core components of the PNA-based Feature Aggregation Block (FAB). Each block combines self-attention (SA) and neighborhood cross-attention (NCA) to jointly model long-range dependencies and local geometric consistency.

3.6 Visual–Language Guidance Module (VLGM)

Even with stronger voxel–voxel reasoning, SSC remains ambiguous in occluded or sparsely observed regions. To inject high-level scene priors—such as road layout, object co-occurrence patterns, or typical urban structures—we introduce the Visual–Language Guidance Module (VLGM). As illustrated in Figure 6, the module leverages a frozen vision–language model (VLM) to produce a free-form scene description, whose textual semantics are encoded and fused into the voxel refinement pipeline.

3.6.1 Text Acquisition and Semantic Encoding

Given an input image I and prompt P , a frozen VLM such as LLaVA Liu et al. (2023a, 2024) or InstructBLIP Dai et al. (2023) generates a scene description

$$T_{\text{text}} = \text{VLM}(I, P),$$

which is precomputed offline to avoid training overhead.

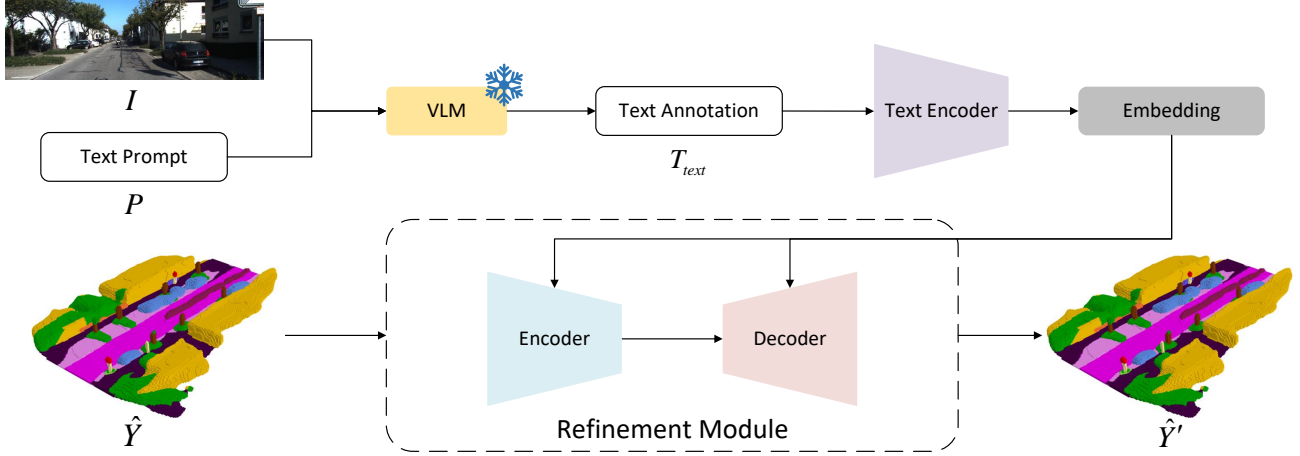


Figure 6. VLGM pipeline. A frozen VLM produces a free-form scene description, which is encoded and fused with voxel features.

To capture different levels of textual semantics, we employ two complementary encoders. (1) **JinaCLIP** Koukounas et al. (2024a,b) extracts a global embedding

$$F_{\text{text}}^{\text{JinaCLIP}} = \text{JinaCLIP}(T_{\text{text}}),$$

providing holistic scene cues. (2) A **Q-Former** Li et al. (2023a) produces token-level embeddings

$$F_{\text{text}}^{\text{Q-Former}} = \text{Q-Former}(T_{\text{text}}),$$

which enable fine-grained cross-modal alignment. This design follows instruction-style prompting practices used in Dai et al. (2023); Liu et al. (2025).

3.6.2 Text–Voxel Fusion Modules

To integrate text cues into voxel refinement, we build a Text U-Net by inserting lightweight fusion blocks after each FEB and FAB. Each fusion block consists of two components:

3.6.2.1 Semantic Interaction Guidance Module (SIGM).

Following Text-IF Yi et al. (2024), global JinaCLIP features are mapped to affine parameters (γ_m, β_m) via MLPs. Voxel features are modulated as

$$F_{\text{out}} = (1 + \gamma_m) \odot F_{\text{in}} + \beta_m,$$

injecting scene-level priors that guide early geometric reasoning.

3.6.2.2 Dual Cross-Attention Module (DCAM).

Inspired by BLIP-2 Li et al. (2023a), SAM Kirillov et al. (2023), and MultiRAtt-RSSC Cai et al. (2024), DCAM alternates self- and cross-attention between Q-Former tokens and voxel features. Text self-attention yields $F_{\text{text}}^{\text{attn}}$, followed by text-to-voxel cross-attention producing $F_{\text{text}}^{\text{enhanced}}$, and voxel-to-text cross-attention generating $F_{\text{voxel}}^{\text{enhanced}}$. A residual update produces

$$F_{\text{out}} = \text{LayerNorm}(F_{\text{voxel}}^{\text{enhanced}} + F_{\text{in}}).$$

SIGM injects global scene priors (e.g., “urban street with parked vehicles”), while DCAM provides fine-grained token-level alignment. As visualized in Figure 6, the two components operate synergistically to improve geometric completeness and semantic coherence, especially in occluded and ambiguous regions.

3.7 Loss Function

ESSC-RM performs coarse-to-fine refinement across multiple spatial scales. We therefore supervise both voxel-wise predictions and scene-level consistency using two complementary terms: a class-weighted cross-entropy loss and the scene-class affinity loss (SCAL) Cao and de Charette (2021); Tang et al. (2023). This combination stabilises multi-scale refinement while encouraging globally coherent semantics.

3.7.1 Cross-Entropy Loss

At each refinement scale l , voxel predictions are supervised using a class-weighted cross-entropy:

$$\mathcal{L}_l = -\frac{1}{C} \sum_{i=0}^N \sum_{c=0}^C w_c y_{i,c} \log \frac{\exp(\hat{y}'_{i,c})}{\sum_{c'=0}^C \exp(\hat{y}'_{i,c'})}, \quad (9)$$

where \hat{y}' denotes refinement logits and w_c compensates for class imbalance Roldão et al. (2020). Aggregating all scales yields:

$$\mathcal{L}_{ce} = \sum_{l=0}^L \mathcal{L}_l. \quad (10)$$

3.7.2 Scene-Class Affinity Loss (SCAL)

To promote globally consistent refinement—particularly under sparsity or ambiguous projections—we adopt SCAL Cao and de Charette (2021), which optimises class-wise precision (P_c), recall (R_c), and specificity (S_c). Let p_i denote the ground-truth class for voxel i , and $\hat{p}_{i,c}$ the predicted probability for class c . Using Iverson brackets $\llbracket \cdot \rrbracket$, the metrics are:

$$P_c(\hat{p}, p) = \log \frac{\sum_i \hat{p}_{i,c} \llbracket p_i = c \rrbracket}{\sum_i \hat{p}_{i,c}}, \quad (11)$$

$$R_c(\hat{p}, p) = \log \frac{\sum_i \hat{p}_{i,c} \llbracket p_i = c \rrbracket}{\sum_i \llbracket p_i = c \rrbracket}, \quad (12)$$

$$S_c(\hat{p}, p) = \log \frac{\sum_i (1 - \hat{p}_{i,c})(1 - \llbracket p_i = c \rrbracket)}{\sum_i (1 - \llbracket p_i = c \rrbracket)}. \quad (13)$$

The per-scale affinity loss is:

$$\mathcal{L}_l(\hat{p}, p) = -\frac{1}{C} \sum_{c=1}^C (P_c(\hat{p}, p) + R_c(\hat{p}, p) + S_c(\hat{p}, p)). \quad (14)$$

SCAL is applied to both semantic and geometric predictions across all refinement scales:

$$\mathcal{L}_{scal}^{sem} = \sum_{l=0}^L \mathcal{L}_l(\hat{y}', y), \quad (15)$$

$$\mathcal{L}_{scal}^{geo} = \sum_{l=0}^L \mathcal{L}_l(\hat{y}'^{geo}, y^{geo}). \quad (16)$$

3.7.3 Overall Objective

The total training loss is:

$$\mathcal{L} = \lambda_{ce} \mathcal{L}_{ce} + \lambda_{scal}^{geo} \mathcal{L}_{scal}^{geo} + \lambda_{scal}^{sem} \mathcal{L}_{scal}^{sem}, \quad (17)$$

with all coefficients set to 1 in our experiments, providing a balanced supervision over voxel-wise accuracy, geometric completion, and scene-level semantic consistency.

4 EXPERIMENT

This section evaluates ESSC-RM on the SemanticKITTI benchmark Behley et al. (2019, 2021). We first describe the experimental setup (datasets, metrics, and implementation), then report quantitative and qualitative results on strong and weak semantic scene completion baselines (CGFormer and MonoScene). Comprehensive ablation studies that analyze the refinement framework, the neighborhood-attention-based aggregation module, and the vision–language guidance module are provided in the supplementary material.

4.1 Experimental Setup

4.1.1 Datasets

We adopt the SemanticKITTI semantic scene completion benchmark Behley et al. (2019, 2021), which extends the KITTI odometry dataset Geiger et al. (2012) with dense semantic labels for each LiDAR scan. The dataset contains 22 outdoor sequences; following the official split, sequences 00–07 and 09–10 are used for training, 08 for validation, and 11–21 as a hidden test set.

For semantic scene completion, a 3D volume around the ego-vehicle is considered: 51.2 m in front, 25.6 m to each side (total width 51.2 m), and 6.4 m in height Behley et al. (2019). This volume is voxelized into a $256 \times 256 \times 32$ grid with voxel size 0.2 m^3 . Each voxel is assigned one of 20 classes (19 semantic classes and 1 free-space), obtained by voxelizing aggregated, registered semantic point clouds Li et al. (2023b).

4.1.2 Evaluation Metrics

We follow standard practice Cao and de Charette (2021); Li et al. (2023b); Tang et al. (2023) and report intersection-over-union (IoU) for 3D scene completion (SC) and mean intersection-over-union (mIoU) for semantic scene completion (SSC).

For SC, evaluation is binary (occupied vs. free) and uses IoU over the occupancy grid:

$$\text{IoU} = \frac{\text{completion_TP}}{\text{completion_TP} + \text{completion_FP} + \text{completion_FN}}, \quad (18)$$

where TP, FP, and FN denote true positives, false positives, and false negatives on the occupancy grid.

For SSC, we evaluate per-class IoU over $C = 19$ semantic classes and report mean IoU:

$$\text{mIoU} = \frac{1}{C} \sum_{c=1}^C \frac{\text{TP}_c}{\text{TP}_c + \text{FP}_c + \text{FN}_c + \epsilon}, \quad (19)$$

where TP_c , FP_c and FN_c are computed for class c , and evaluation is carried out in known space as in Roldao et al. (2021). IoU primarily reflects geometric completion quality, whereas mIoU captures voxel-wise semantic accuracy; both are reported to assess overall scene understanding.

4.1.3 Implementation Details

We consider two training paradigms for ESSC-RM: (1) joint training, where the semantic scene completion backbone is switched to inference mode while the refinement module is trained on-the-fly from its predictions; and (2) separate training, where semantic scene completion predictions are pre-computed and stored, and the refinement module is trained purely as a plug-and-play post-processor without modifying the original semantic scene completion architecture.

Unless otherwise stated, experiments are conducted on two NVIDIA RTX A5000 GPUs, with 10 epochs and a batch size of 1 per GPU. We use AdamW Loshchilov and Hutter (2017) with $\beta_1 = 0.9$, $\beta_2 = 0.99$, and a peak learning rate of 5×10^{-5} . A cosine schedule Smith and Topin (2017) with 5% warm-up is applied. The refinement module follows a 3D U-Net Çiçek et al. (2016) backbone; encoder and decoder feature-enhancement blocks (FEB/FAB) are adapted from SemCity Lee et al. (2024), and neighborhood-attention-based variants from NATTEN Hassani and Shi (2022); Hassani et al. (2023, 2024) and PNA Liu et al. (2023c). The vision–language guidance module (VLGM) uses frozen vision–language

models (InstructBLIP Li et al. (2023a); Dai et al. (2023) and LLaVA Liu et al. (2023a, 2024)) together with text–voxel fusion modules inspired by Text-IF Yi et al. (2024) and MultiAtt-RSSC Cai et al. (2024). Following PaSCo Cao et al. (2024a) and HybridOcc Zhao et al. (2024b), we apply coarse-to-fine multi-level supervision in the decoder. Training losses are described in Sec. 3.7.

4.2 Evaluation Results

We evaluate ESSC-RM as a refinement module on strong and weak SSC baselines and analyze its efficiency and qualitative behavior.

4.2.1 Quantitative Results

4.2.1.1 3D SSC performance.

Table 1 reports SSC performance of representative stereo-based methods and our ESSC-RM variants on SemanticKITTI. Among the methods without ESSC-RM (all rows whose method name does not contain “+”), CGFormer Tang et al. (2023) achieves the highest IoU and mIoU (45.99% IoU and 16.87% mIoU), while MonoScene Cao and de Charette (2021) provides a weaker yet widely used baseline (36.86% IoU, 11.08% mIoU).

Methods	IoU	mIoU																				
			car (3.92%)	bicycle (0.03%)	motorcycle (0.03%)	truck (0.16%)	other-vehicle (0.20%)	person (0.07%)	bicyclist (0.07%)	motorcyclist (0.05%)	road (15.30%)	parking (1.12%)	sidewalk (11.13%)	other-ground (0.56%)	building (14.10%)	fence (3.90%)	vegetation (39.3%)	trunk (0.51%)	terrain (9.17%)	pole (0.29%)	traffic-sign (0.08%)	
<i>Baselines (without ESSC-RM)</i>																						
TPVFormer Huang et al. (2023)	35.61	11.36	23.81	0.36	0.05	8.08	4.35	0.51	0.89	0.00	56.50	20.60	25.87	0.85	13.88	5.94	16.92	2.26	30.38	3.14	1.52	
OccFormer Zhang et al. (2023)	36.50	13.46	25.09	0.81	<u>1.19</u>	25.53	<u>8.52</u>	2.78	2.82	0.00	58.85	<u>19.61</u>	26.88	0.31	14.40	5.61	19.63	3.93	32.62	4.26	2.86	
IAMSSC Xiao et al. (2024)	44.29	12.45	26.26	0.60	0.15	8.74	5.06	1.32	3.46	0.01	54.55	16.02	25.85	0.70	17.38	6.86	24.63	4.95	30.13	6.35	3.56	
VoxFormer-S Li et al. (2023b)	44.02	12.35	25.79	0.59	0.51	5.63	3.77	1.78	3.32	0.00	54.76	15.50	26.35	0.70	17.65	7.64	24.39	5.08	29.96	7.11	4.18	
DepthSCS Yao et al. (2024)	45.84	13.28	25.94	0.35	1.16	6.02	7.50	2.58	6.32	0.00	55.38	18.76	27.04	0.92	19.23	8.46	26.37	4.52	30.19	7.42	4.09	
Syphonize Jiang et al. (2023)	41.92	14.89	28.68	2.54	2.82	<u>20.44</u>	13.89	3.52	2.24	0.00	56.37	15.28	27.58	<u>0.95</u>	21.64	<u>8.40</u>	25.72	<u>6.60</u>	30.87	9.57	5.76	
HASSC-S Wang et al. (2024)	<u>44.82</u>	13.48	27.23	<u>0.92</u>	0.86	9.91	5.61	<u>2.80</u>	<u>4.71</u>	0.00	<u>57.05</u>	15.90	<u>28.25</u>	1.04	19.05	6.58	25.48	6.15	<u>32.94</u>	7.68	4.05	
H2GFormer-S Wang and Tong (2024)	44.57	<u>13.73</u>	<u>28.21</u>	0.50	0.47	10.00	7.39	1.54	2.88	<u>0.00</u>	56.08	17.83	29.12	0.45	<u>19.74</u>	7.24	<u>26.25</u>	6.80	34.42	<u>7.88</u>	<u>4.68</u>	
<i>MonoScene and ESSC-RM variants</i>																						
MonoScene Cao and de Charette (2021)	36.86	11.08	<u>23.26</u>	0.61	0.45	6.98	1.48	1.86	1.20	0.00	56.52	14.27	26.72	0.46	14.09	5.84	17.89	2.81	29.64	4.14	2.25	
MonoScene + 3D U-Net	35.70	11.47	23.46	0.41	0.87	10.95	3.69	<u>2.98</u>	<u>1.64</u>	0.00	56.24	14.95	26.63	<u>1.42</u>	13.11	6.19	16.75	2.73	<u>29.57</u>	3.77	2.62	
MonoScene + VLGM	35.62	<u>11.49</u>	22.76	<u>0.44</u>	0.71	12.45	3.12	3.04	<u>1.64</u>	0.00	<u>56.48</u>	14.35	26.64	<u>1.42</u>	<u>13.55</u>	6.28	16.44	2.97	29.50	<u>3.85</u>	<u>2.65</u>	
MonoScene + PNAM	<u>36.44</u>	11.51	23.11	0.40	<u>0.73</u>	11.38	<u>3.59</u>	2.95	1.69	0.00	56.27	<u>14.65</u>	<u>26.71</u>	1.45	13.48	6.20	17.08	<u>2.96</u>	29.45	3.84	2.69	
<i>CGFormer and ESSC-RM variants</i>																						
CGFormer Tang et al. (2023)	45.99	16.87	<u>34.32</u>	4.61	2.71	19.44	7.67	2.38	4.08	0.00	<u>65.51</u>	<u>20.82</u>	32.31	<u>0.16</u>	23.52	9.20	26.93	8.83	39.54	10.67	7.84	
CGFormer + 3D U-Net	43.53	17.17	33.99	<u>5.28</u>	3.11	<u>22.39</u>	<u>8.22</u>	<u>2.65</u>	4.05	0.00	65.29	20.26	<u>32.14</u>	<u>0.13</u>	23.11	8.93	<u>26.84</u>	<u>11.17</u>	38.99	11.93	7.84	
CGFormer + VLGM	43.20	<u>17.21</u>	34.33	5.24	<u>3.01</u>	22.33	7.81	2.70	<u>4.12</u>	0.00	65.52	20.79	32.31	<u>0.13</u>	<u>23.27</u>	8.95	26.69	10.73	<u>39.29</u>	11.93	<u>7.82</u>	
CGFormer + PNAM	<u>44.33</u>	17.27	34.11	<u>5.69</u>	2.94	23.71	<u>8.36</u>	2.64	<u>4.37</u>	0.00	65.27	20.87	31.90	<u>0.16</u>	22.70	<u>9.08</u>	26.63	<u>11.42</u>	38.91	<u>11.78</u>	7.66	

Table 1. Quantitative results on the SemanticKITTI validation set. The upper block lists baseline stereo-based SSC methods without ESSC-RM. The middle and lower blocks show MonoScene- and CGFormer-based ESSC-RM variants, respectively. Within each block, the best and second-best results are shown in **bold** and underlined, respectively.

To assess the generality of ESSC-RM, we plug it on top of both CGFormer and MonoScene, progressively adding (i) a plain 3D U-Net refinement head, (ii) the proposed neighborhood-attention-based refinement module (PNAM), and (iii) the vision–language guidance module (VLGM). The MonoScene and CGFormer blocks in Table 1 summarize these ablation results.

4.2.1.2 ESSC-RM on CGFormer.

As shown in the CGFormer block of Table 1, adding a 3D U-Net refinement head already improves mIoU from 16.87% to 17.17%. Introducing VLGM further boosts mIoU to 17.21%, while PNAM obtains the best mIoU of 17.27% with only a modest IoU drop. Gains are particularly visible on small and medium-scale categories (for example, truck, bicycle, trunk, pole), indicating that coarse-to-fine refinement and neighborhood attention help recover fine structures and ambiguous regions that are challenging for the backbone alone.

4.2.1.3 ESSC-RM on MonoScene.

The MonoScene block of Table 1 shows that ESSC-RM also improves the weaker MonoScene baseline. VLGM increases mIoU from 11.08% to 11.49%, largely by enhancing medium-scale categories such as truck, while PNAM further pushes mIoU to 11.51% with comparable IoU. This confirms that ESSC-RM is not tailored to a specific architecture; it consistently benefits both strong and weak SSC backbones.

Although refinement improves mIoU, IoU can slightly decrease, especially when the backbone predictions are already geometrically plausible. This is expected: ESSC-RM operates on discrete voxel predictions without direct access to LiDAR depth, and thus focuses more on semantic correction than on large-scale geometric restructuring.

4.2.1.4 Refinement module efficiency.

We further analyze the computational overhead of ESSC-RM on top of CGFormer (Table 2). CGFormer itself has 122.42M parameters, requires about 19.3 GB memory during training and 6.55 GB at inference, and runs at approximately 205 ms per frame. The 3D U-Net refinement head adds only 13.36M parameters and can be trained jointly with CGFormer on a 24GB GPU when the backbone is set to inference mode. VLGM and PNAM increase parameter counts and inference time more noticeably, but remain practical for offline refinement or two-stage pipelines.

Model	IoU	mIoU	Params (M)	Train Memory (M)	Infer. Memory (M)	Infer. Time (ms)
CGFormer	45.99	16.87	122.42	19330	6550	205
+3D U-Net	43.53	17.17	13.36	12726	4904	215
+VLGM	43.20	17.21	43.96	18942	5382	340
+PNAM	44.33	17.27	9.59	20664	5042	265

Table 2. Ablation study on the efficiency of the refinement module with CGFormer as backbone.

4.2.2 Qualitative Results

Figures 7 and 8 present qualitative results of ESSC-RM applied respectively to CGFormer and MonoScene on the SemanticKITTI validation set. Each row displays the input RGB image, ground truth, the prediction of the baseline model, and the refined outputs after integrating the 3D U-Net, PNAM, and VLGM modules.

Across both baselines, the refinement module consistently reduces holes and misclassifications in occluded or boundary regions, restores missing vegetation and structures at scene edges, and produces smoother and more coherent semantic layouts. On large-scale structures such as roads and buildings, PNAM and VLGM further improve geometric regularity, yielding cleaner contours and more stable surface predictions. For small-scale objects like traffic signs and poles, text-derived priors in VLGM highlight distinctive semantic regions, while PNAM enhances local aggregation and sharpens object boundaries.

These results demonstrate that ESSC-RM provides robust and generalizable refinement across different SSC backbones.

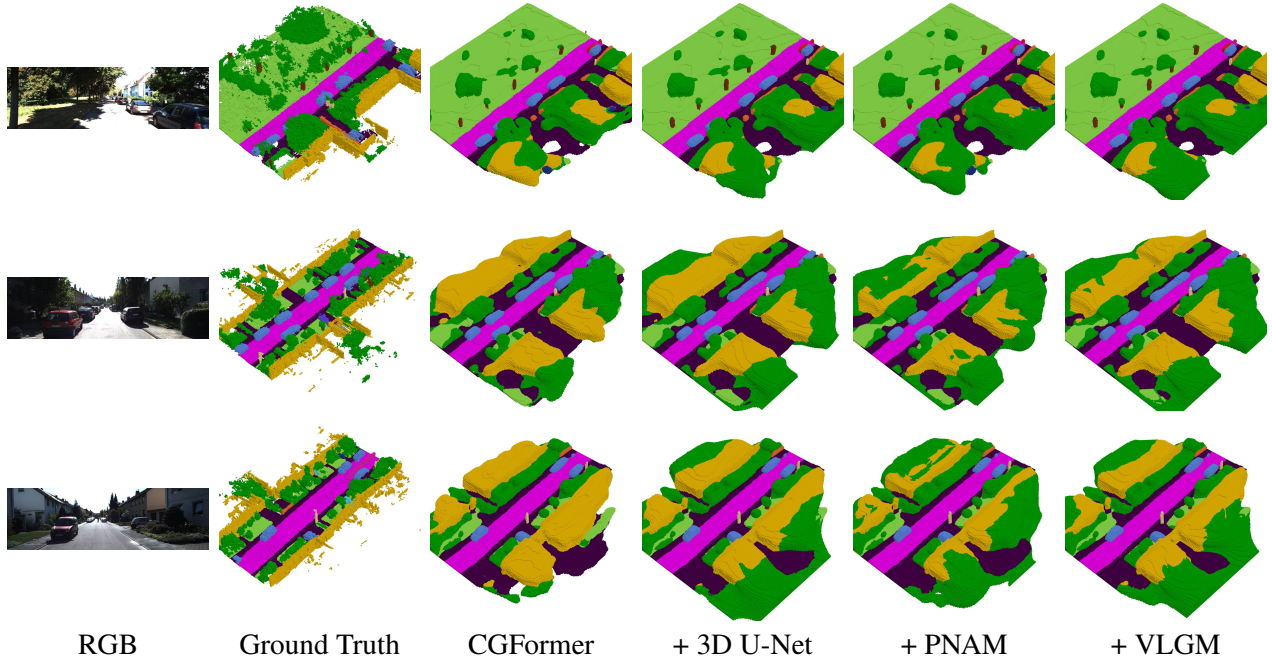


Figure 7. Qualitative results of ESSC-RM on CGFormer Tang et al. (2023) on the SemanticKITTI Behley et al. (2019, 2021) validation set. ESSC-RM progressively refines the baseline prediction, filling missing regions and improving object shapes and small semantic structures.

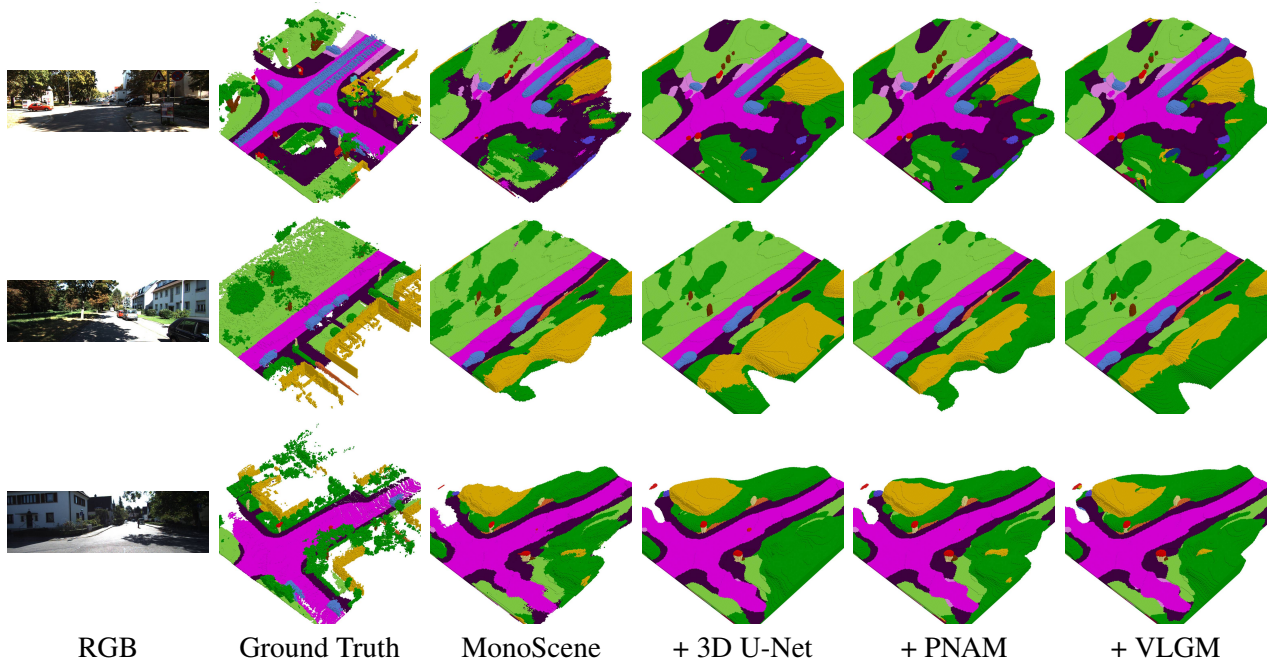


Figure 8. Qualitative results of ESSC-RM on MonoScene Cao and de Charette (2021) on the SemanticKITTI Behley et al. (2019, 2021) validation set. ESSC-RM enhances the baseline prediction by completing missing structures, improving geometric consistency, and sharpening small semantic objects.

5 CONCLUSION

In summary, although ESSC-RM substantially improves semantic scene completion by refining voxel features with PNAM and VLGM, several challenges remain. The current refinement module relies heavily on 3D convolutions and attention, resulting in non-negligible latency and memory overhead, while the

dependence on SemanticKITTI limits cross-dataset generalization. Moreover, the plug-and-play property is constrained because voxel resolutions, label taxonomies, and scene layouts vary across datasets, requiring re-training and structural adjustments. PNAM and VLGM also operate as relatively independent components without a unified fusion mechanism, and the focus on semantic reconstruction may compromise geometric completeness, causing minor degradations in SC-IoU. Future work will thus explore lightweight and efficient representations (e.g., sparse convolution, tri-plane features, Gaussian voxelization), knowledge distillation for compact deployment, adapter-based generalization across datasets, and adaptive fusion layers that jointly leverage local geometric attention and textual semantics. Additionally, integrating generative models (e.g., CVAE or diffusion priors) to pre-complete sparse voxels, combined with extensive evaluations on diverse real-world datasets, will further improve the robustness, practicality, and scalability of ESSC-RM.

6 ACKNOWLEDGMENTS

This research was funded by the Natural Science Foundation of Tianjin (No. 24PTLYHZ00290).

REFERENCES

Behley, J., Garbade, M., Milioto, A., Quenzel, J., Behnke, S., Gall, J., et al. (2021). Towards 3d lidar-based semantic scene understanding of 3d point cloud sequences: The semantickitti dataset. *The International Journal of Robotics Research* 40, 959–967. doi:10.1177/02783649211006735

Behley, J., Garbade, M., Milioto, A., Quenzel, J., Behnke, S., Stachniss, C., et al. (2019). A dataset for semantic segmentation of point cloud sequences. *CoRR* abs/1904.01416

Brazil, G. and Liu, X. (2019). M3D-RPN: monocular 3d region proposal network for object detection. *CoRR* abs/1907.06038

[Dataset] Cai, J., Meng, K., Yang, B., and Shao, G. (2024). Multimodal remote sensing scene classification using vlms and dual-cross attention networks

Cao, A. and de Charette, R. (2021). Monoscene: Monocular 3d semantic scene completion. *CoRR* abs/2112.00726

[Dataset] Cao, A.-Q., Dai, A., and de Charette, R. (2024a). Pasco: Urban 3d panoptic scene completion with uncertainty awareness

Cao, H., Chen, G., Li, Z., Hu, Y., and Knoll, A. (2022). Neurograsp: Multimodal neural network with euler region regression for neuromorphic vision-based grasp pose estimation. *IEEE Transactions on Instrumentation and Measurement* 71, 1–11. doi:10.1109/TIM.2022.3179469

Cao, H., Chen, G., Xia, J., Zhuang, G., and Knoll, A. (2021). Fusion-based feature attention gate component for vehicle detection based on event camera. *IEEE Sensors Journal* 21, 24540–24548. doi:10.1109/JSEN.2021.3115016

Cao, H., Chen, G., Zhao, H., Jiang, D., Zhang, X., Tian, Q., et al. (2024b). Sdpt: Semantic-aware dimension-pooling transformer for image segmentation. *IEEE Transactions on Intelligent Transportation Systems* 25, 15934–15946. doi:10.1109/TITS.2024.3417813

Cao, H., Qu, Z., Chen, G., Li, X., Thiele, L., and Knoll, A. (2024c). Ghostvit: Expediting vision transformers via cheap operations. *IEEE Transactions on Artificial Intelligence* 5, 2517–2525. doi:10.1109/TAI.2023.3326795

Cao, H., Zhang, Z., Xia, Y., Li, X., Xia, J., Chen, G., et al. (2024d). Embracing events and frames with hierarchical feature refinement network for object detection. In *European Conference on Computer Vision* (Springer), 161–177

Chang, J. and Chen, Y. (2018). Pyramid stereo matching network. *CoRR* abs/1803.08669

Chen, Y., Liu, S., Shen, X., and Jia, J. (2020). DSGN: deep stereo geometry network for 3d object detection. *CoRR* abs/2001.03398

Cho, M. and Kim, E. (2023). 3d lidar multi-object tracking with short-term and long-term multi-level associations. *Remote Sensing* 15. doi:10.3390/rs15235486

Çiçek, Ö., Abdulkadir, A., Lienkamp, S. S., Brox, T., and Ronneberger, O. (2016). 3d u-net: Learning dense volumetric segmentation from sparse annotation. *CoRR* abs/1606.06650

[Dataset] Dai, W., Li, J., Li, D., Tiong, A. M. H., Zhao, J., Wang, W., et al. (2023). Instructblip: Towards general-purpose vision-language models with instruction tuning

Deng, J., Shi, S., Li, P., Zhou, W., Zhang, Y., and Li, H. (2020). Voxel R-CNN: towards high performance voxel-based 3d object detection. *CoRR* abs/2012.15712

Doll, S., Schulz, R., Schneider, L., Benzin, V., Markus, E., and Lensch, H. P. (2022). Spatialdetr: Robust scalable transformer-based 3d object detection from multi-view camera images with global cross-sensor attention. In *European Conference on Computer Vision (ECCV)*

Duan, K., Bai, S., Xie, L., Qi, H., Huang, Q., and Tian, Q. (2019). Centernet: Keypoint triplets for object detection. *CoRR* abs/1904.08189

Geiger, A., Lenz, P., and Urtasun, R. (2012). Are we ready for autonomous driving? the kitti vision benchmark suite. In *2012 IEEE Conference on Computer Vision and Pattern Recognition*. 3354–3361. doi:10.1109/CVPR.2012.6248074

Guo, Y., Wang, H., Hu, Q., Liu, H., Liu, L., and Bennamoun, M. (2019). Deep learning for 3d point clouds: A survey. *CoRR* abs/1912.12033

Hassani, A., Hwu, W.-M., and Shi, H. (2024). Faster neighborhood attention: Reducing the $o(n^2)$ cost of self attention at the threadblock level. In *Advances in Neural Information Processing Systems*

[Dataset] Hassani, A. and Shi, H. (2022). Dilated neighborhood attention transformer

Hassani, A., Walton, S., Li, J., Li, S., and Shi, H. (2023). Neighborhood attention transformer. In *IEEE/CVF Conference on Computer Vision and Pattern Recognition (CVPR)*

Hu, H., Cai, Q., Wang, D., Lin, J., Sun, M., Krähenbühl, P., et al. (2018). Joint monocular 3d vehicle detection and tracking. *CoRR* abs/1811.10742

Huang, J., Huang, G., Zhu, Z., and Du, D. (2021). Bevdet: High-performance multi-camera 3d object detection in bird-eye-view. *CoRR* abs/2112.11790

[Dataset] Huang, Y., Zheng, W., Zhang, Y., Zhou, J., and Lu, J. (2023). Tri-perspective view for vision-based 3d semantic occupancy prediction

[Dataset] Jang, H.-K., Kim, J., Kweon, H., and Yoon, K.-J. (2024). Talos: Enhancing semantic scene completion via test-time adaptation on the line of sight

[Dataset] Jiang, H., Cheng, T., Gao, N., Zhang, H., Lin, T., Liu, W., et al. (2023). Symphonize 3d semantic scene completion with contextual instance queries

Kirillov, A., Mintun, E., Ravi, N., Mao, H., Rolland, C., Gustafson, L., et al. (2023). Segment anything. *arXiv:2304.02643*

[Dataset] Koukounas, A., Mastrapas, G., Günther, M., Wang, B., Martens, S., Mohr, I., et al. (2024a). Jina clip: Your clip model is also your text retriever

[Dataset] Koukounas, A., Mastrapas, G., Wang, B., Akram, M. K., Eslami, S., Günther, M., et al. (2024b). jina-clip-v2: Multilingual multimodal embeddings for text and images

Lang, A. H., Vora, S., Caesar, H., Zhou, L., Yang, J., and Beijbom, O. (2018). Pointpillars: Fast encoders for object detection from point clouds. *CoRR* abs/1812.05784

[Dataset] Lee, J., Lee, S., Jo, C., Im, W., Seon, J., and Yoon, S.-E. (2024). Semcity: Semantic scene generation with triplane diffusion

Li, B., Weinberger, K. Q., Belongie, S. J., Koltun, V., and Ranftl, R. (2022a). Language-driven semantic segmentation. *CoRR* abs/2201.03546

[Dataset] Li, J., Li, D., Savarese, S., and Hoi, S. (2023a). Blip-2: Bootstrapping language-image pre-training with frozen image encoders and large language models

Li, P., Chen, X., and Shen, S. (2019). Stereo R-CNN based 3d object detection for autonomous driving. *CoRR* abs/1902.09738

[Dataset] Li, S. and Tang, H. (2024). Multimodal alignment and fusion: A survey

[Dataset] Li, Y., Li, S., Liu, X., Gong, M., Li, K., Chen, N., et al. (2024). Sscbench: A large-scale 3d semantic scene completion benchmark for autonomous driving

[Dataset] Li, Y., Yu, Z., Choy, C., Xiao, C., Alvarez, J. M., Fidler, S., et al. (2023b). Voxformer: Sparse voxel transformer for camera-based 3d semantic scene completion

[Dataset] Li, Z., Wang, W., Li, H., Xie, E., Sima, C., Lu, T., et al. (2022b). Bevformer: Learning bird's-eye-view representation from multi-camera images via spatiotemporal transformers

Lin, S.-L. and Wu, J.-Y. (2025). Enhancing lidar-based 3d classification through an improved deep learning framework with residual connections. *IEEE Access* 13, 42836–42849. doi:10.1109/ACCESS.2025.3547942

[Dataset] Liu, H., Li, C., Li, Y., and Lee, Y. J. (2024). Improved baselines with visual instruction tuning

[Dataset] Liu, H., Li, C., Wu, Q., and Lee, Y. J. (2023a). Visual instruction tuning

[Dataset] Liu, P., Liu, H., Liu, H., Liu, X., Ni, J., and Ma, J. (2025). Vlm-e2e: Enhancing end-to-end autonomous driving with multimodal driver attention fusion

Liu, S., Zeng, Z., Ren, T., Li, F., Zhang, H., Yang, J., et al. (2023b). Grounding dino: Marrying dino with grounded pre-training for open-set object detection. *arXiv preprint arXiv:2303.05499*

Liu, T., Wei, Y., and Zhang, Y. (2023c). Progressive neighborhood aggregation for semantic segmentation refinement. In *Proceedings of the Thirty-Seventh AAAI Conference on Artificial Intelligence and Thirty-Fifth Conference on Innovative Applications of Artificial Intelligence and Thirteenth Symposium on Educational Advances in Artificial Intelligence* (AAAI Press), AAAI'23/IAAI'23/EAAI'23. doi:10.1609/aaai.v37i2.25262

Loshchilov, I. and Hutter, F. (2017). Fixing weight decay regularization in adam. *CoRR* abs/1711.05101

Ma, X., Ouyang, W., Simonelli, A., and Ricci, E. (2022). 3d object detection from images for autonomous driving: A survey. *CoRR* abs/2202.02980

Manhardt, F., Kehl, W., and Gaidon, A. (2018). ROI-10D: monocular lifting of 2d detection to 6d pose and metric shape. *CoRR* abs/1812.02781

[Dataset] Mao, J., Shi, S., Wang, X., and Li, H. (2023). 3d object detection for autonomous driving: A comprehensive survey

Milioto, A., Vizzo, I., Behley, J., and Stachniss, C. (2019). Rangenet ++: Fast and accurate lidar semantic segmentation. In *2019 IEEE/RSJ International Conference on Intelligent Robots and Systems (IROS)*. 4213–4220. doi:10.1109/IROS40897.2019.8967762

Mousavian, A., Anguelov, D., Flynn, J., and Kosecka, J. (2016). 3d bounding box estimation using deep learning and geometry. *CoRR* abs/1612.00496

[Dataset] OpenAI, Achiam, J., Adler, S., Agarwal, S., Ahmad, L., Akkaya, I., et al. (2024). Gpt-4 technical report

Phlion, J. and Fidler, S. (2020). Lift, splat, shoot: Encoding images from arbitrary camera rigs by implicitly unprojecting to 3d. *CoRR* abs/2008.05711

Qi, C. R., Su, H., Mo, K., and Guibas, L. J. (2016). Pointnet: Deep learning on point sets for 3d classification and segmentation. *CoRR* abs/1612.00593

Qi, C. R., Yi, L., Su, H., and Guibas, L. J. (2017). Pointnet++: Deep hierarchical feature learning on point sets in a metric space. *CoRR* abs/1706.02413

Radford, A., Kim, J. W., Hallacy, C., Ramesh, A., Goh, G., Agarwal, S., et al. (2021). Learning transferable visual models from natural language supervision. *CoRR* abs/2103.00020

[Dataset] Ren, T., Liu, S., Zeng, A., Lin, J., Li, K., Cao, H., et al. (2024). Grounded sam: Assembling open-world models for diverse visual tasks

Roldão, L., de Charette, R., and Verroust-Blondet, A. (2020). Lmscnet: Lightweight multiscale 3d semantic completion. *CoRR* abs/2008.10559

Roldao, L., de Charette, R., and Verroust-Blondet, A. (2021). 3d semantic scene completion: a survey. *CoRR* abs/2103.07466

Ronneberger, O., Fischer, P., and Brox, T. (2015). U-net: Convolutional networks for biomedical image segmentation. *CoRR* abs/1505.04597

Shi, S., Guo, C., Jiang, L., Wang, Z., Shi, J., Wang, X., et al. (2019). PV-RCNN: point-voxel feature set abstraction for 3d object detection. *CoRR* abs/1912.13192

Shi, S., Wang, X., and Li, H. (2018). Pointrcnn: 3d object proposal generation and detection from point cloud. *CoRR* abs/1812.04244

Silberman, N., Hoiem, D., Kohli, P., and Fergus, R. (2012). Indoor segmentation and support inference from rgbd images. In *Computer Vision – ECCV 2012*, eds. A. Fitzgibbon, S. Lazebnik, P. Perona, Y. Sato, and C. Schmid (Berlin, Heidelberg: Springer Berlin Heidelberg), 746–760

Smith, L. N. and Topin, N. (2017). Super-convergence: Very fast training of residual networks using large learning rates. *CoRR* abs/1708.07120

Song, S., Yu, F., Zeng, A., Chang, A. X., Savva, M., and Funkhouser, T. A. (2016). Semantic scene completion from a single depth image. *CoRR* abs/1611.08974

[Dataset] Sun, Q., Fang, Y., Wu, L., Wang, X., and Cao, Y. (2023). Eva-clip: Improved training techniques for clip at scale

[Dataset] Sun, Q., Wang, J., Yu, Q., Cui, Y., Zhang, F., Zhang, X., et al. (2024). Eva-clip-18b: Scaling clip to 18 billion parameters

[Dataset] Tang, J., Zheng, G., Shi, C., and Yang, S. (2023). Contrastive grouping with transformer for referring image segmentation

Ulyanov, D., Vedaldi, A., and Lempitsky, V. S. (2016). Instance normalization: The missing ingredient for fast stylization. *CoRR* abs/1607.08022

Vaswani, A., Shazeer, N., Parmar, N., Uszkoreit, J., Jones, L., Gomez, A. N., et al. (2017). Attention is all you need. *CoRR* abs/1706.03762

[Dataset] Wang, M., Pi, H., Li, R., Qin, Y., Tang, Z., and Li, K. (2025a). Vlscene: Vision-language guidance distillation for camera-based 3d semantic scene completion

[Dataset] Wang, M., Wu, F., Qin, Y., Li, R., Tang, Z., and Li, K. (2025b). Vision-based 3d semantic scene completion via capture dynamic representations

[Dataset] Wang, S., Yu, J., Li, W., Liu, W., Liu, X., Chen, J., et al. (2024). Not all voxels are equal: Hardness-aware semantic scene completion with self-distillation

Wang, Y., Chao, W., Garg, D., Hariharan, B., Campbell, M., and Weinberger, K. Q. (2018). Pseudo-lidar from visual depth estimation: Bridging the gap in 3d object detection for autonomous driving. *CoRR* abs/1812.07179

Wang, Y., Guizilini, V., Zhang, T., Wang, Y., Zhao, H., and Solomon, J. (2021). DETR3D: 3d object detection from multi-view images via 3d-to-2d queries. *CoRR* abs/2110.06922

Wang, Y. and Tong, C. (2024). H2gformer: Horizontal-to-global voxel transformer for 3d semantic scene completion. *Proceedings of the AAAI Conference on Artificial Intelligence* 38, 5722–5730. doi:10.1609/aaai.v38i6.28384

Weng, X., Wang, J., Held, D., and Kitani, K. (2020). AB3DMOT: A baseline for 3d multi-object tracking and new evaluation metrics. *CoRR* abs/2008.08063

Wu, D., Liang, Z., and Chen, G. (2022). Deep learning for lidar-only and lidar-fusion 3d perception: a survey. *Intelligence & Robotics* 2. doi:10.20517/ir.2021.20

[Dataset] Xia, Z., Liu, Y., Li, X., Zhu, X., Ma, Y., Li, Y., et al. (2023). Scpnet: Semantic scene completion on point cloud

Xiao, H., Xu, H., Kang, W., and Li, Y. (2024). Instance-aware monocular 3d semantic scene completion. *IEEE Transactions on Intelligent Transportation Systems* 25, 6543–6554. doi:10.1109/TITS.2023.3344806

Xu, B. and Chen, Z. (2018). Multi-level fusion based 3d object detection from monocular images. In *2018 IEEE/CVF Conference on Computer Vision and Pattern Recognition*. 2345–2353. doi:10.1109/CVPR.2018.00249

Xu, B., Wang, N., Chen, T., and Li, M. (2015). Empirical evaluation of rectified activations in convolutional network. *CoRR* abs/1505.00853

Xu, X., Wang, T., Yang, Y., Zuo, L., Shen, F., and Shen, H. T. (2020). Cross-modal attention with semantic consistence for image–text matching. *IEEE Transactions on Neural Networks and Learning Systems* 31, 5412–5425. doi:10.1109/TNNLS.2020.2967597

Yan, X., Gao, J., Li, J., Zhang, R., Li, Z., Huang, R., et al. (2020). Sparse single sweep lidar point cloud segmentation via learning contextual shape priors from scene completion. *CoRR* abs/2012.03762

Yan, Y., Mao, Y., and Li, B. (2018). Second: Sparsely embedded convolutional detection. *Sensors* 18. doi:10.3390/s18103337

Yang, X., Zou, H., Kong, X., Huang, T., Liu, Y., Li, W., et al. (2021). Semantic segmentation-assisted scene completion for lidar point clouds. *CoRR* abs/2109.11453

[Dataset] Yao, J., Zhang, J., Pan, X., Wu, T., and Xiao, C. (2024). Depthssc: Monocular 3d semantic scene completion via depth-spatial alignment and voxel adaptation

[Dataset] Yi, X., Xu, H., Zhang, H., Tang, L., and Ma, J. (2024). Text-if: Leveraging semantic text guidance for degradation-aware and interactive image fusion

You, Y., Wang, Y., Chao, W., Garg, D., Pleiss, G., Hariharan, B., et al. (2019). Pseudo-lidar++: Accurate depth for 3d object detection in autonomous driving. *CoRR* abs/1906.06310

Yurtsever, E., Lambert, J., Carballo, A., and Takeda, K. (2020). A survey of autonomous driving: Common practices and emerging technologies. *IEEE Access* 8, 58443–58469. doi:10.1109/ACCESS.2020.2983149

[Dataset] Zhang, B., Zhang, P., Dong, X., Zang, Y., and Wang, J. (2024). Long-clip: Unlocking the long-text capability of clip

[Dataset] Zhang, Y., Zhu, Z., and Du, D. (2023). Occformer: Dual-path transformer for vision-based 3d semantic occupancy prediction

Zhao, H., Li, X., Xu, C., Xu, B., and Liu, H. (2024a). A survey of automatic driving environment perception. In *2024 IEEE 24th International Conference on Software Quality, Reliability, and Security Companion (QRS-C)*. 1038–1047. doi:10.1109/QRS-C63300.2024.00137

Zhao, X., Chen, B., Sun, M., Yang, D., Wang, Y., Zhang, X., et al. (2024b). Hybridocc: Nerf enhanced transformer-based multi-camera 3d occupancy prediction. *IEEE Robotics and Automation Letters* 9, 7867–7874. doi:10.1109/lra.2024.3416798

Zhou, H., Zhu, X., Song, X., Ma, Y., Wang, Z., Li, H., et al. (2020). Cylinder3d: An effective 3d framework for driving-scene lidar semantic segmentation. *CoRR* abs/2008.01550

Zhou, Y. and Tuzel, O. (2017). Voxelnet: End-to-end learning for point cloud based 3d object detection. *CoRR* abs/1711.06396

[Dataset] Zhu, D., Chen, J., Shen, X., Li, X., and Elhoseiny, M. (2023). Minigpt-4: Enhancing vision-language understanding with advanced large language models

Zia, M. Z., Stark, M., and Schindler, K. (2014). Are cars just 3d boxes? jointly estimating the 3d shape of multiple objects. In *2014 IEEE Conference on Computer Vision and Pattern Recognition*. 3678–3685. doi:10.1109/CVPR.2014.470